Biosensors and Bioelectronics 159 (2020) 112201

Contents lists available at ScienceDirect

Biosensors and Bioelectronics

journal homepage: http://www.elsevier.com/locate/bios

# Design and application of proximity hybridization-based multiple stimuli-responsive immunosensing platform for ovarian cancer biomarker detection

Shupei Zhang [a,b,1], Yanjie Chen [a,1], Yitian Huang [a], Hong Dai [a,b,*], Yanyu Lin [a]

[a] College of Chemistry and Materials, Fujian Normal University, Fuzhou, Fujian, 350108, China
[b] Fujian Provincial Maternity and Children Hospital, Fuzhou, Fujian, 350108, China

ARTICLE INFO

*Keywords:*
Multi-readout immunoassay
Electrochemiluminescence
Temperature sensing
Colorimetric system
Proximity hybridization

ABSTRACT

The development of convenient and sensitive multi-readout immunoassay is crucial but highly challenged for meeting the demand of exactness and diversity in early clinical diagnosis. Herein, a split-type multiple stimuli-responsive biosensor was outlined combined with the outstanding superiority of luminol probe-based electrochemiluminescence (ECL) strategy, mimicking enzyme-mediated colorimetric system and portable photothermal effect-induced temperature sensing. Especially, versatile $MoS_2$ nanosheets ($MoS_2$ NSs) with distinguished property not only acted as dual-promoter to improve the cathodic ECL of luminol because of its good electrocatalytic activity for dissolved $O_2$ and favorable photothermal effect for elevating electrode temperature, but also used as nanozyme to regulate subsequent split-type visual colorimetric sensing due to its peroxidase-like activity for the generation of oxidized 2,2′-azinobis(3-ethylbenzothiazoline)-6-sulfonic acid (ABTS) in ABTS-$H_2O_2$ colorimetric system. More importantly, the green oxidized ABTS ($ABTS^{\bullet+}$) also exhibited strong near-infrared (NIR) laser-triggered photothermal performance, which can be innovatively employed as sensitive photothermal agent for converting biological signals into temperature under the irradiation of NIR laser, accomplishing more simpler temperature quantitative detection by a portable thermometer. Furthermore, on account of the affinity discrepancy of $MoS_2$ NSs to single-stranded and double-stranded nucleic acids, a label-free proximity hybridization-based multifunctional assay platform was proposed for target detection with human epididymis-specific protein 4 (HE4) as model protein, demonstrating good analytical performances. Significantly, this innovative work not only enriches the foundational study of multi-model biosensing based on the unitary material but also provides an unambiguous guideline for exploring more accurate and simpler point-of-care diagnosis.

## 1. Introduction

Simple, rapid, and specific detection of proteins, in particular, tumor markers, is significant for point-of-care testing (POCT) in clinical disease prediction, diagnosis and evaluation (Liu et al., 2019a; Gao et al., 2017). Immunoassay is the dominant analytical strategy for biomarker protein quantitative analysis because of the highly specific recognition between antigen and antibody (Li et al., 2013). Despite traditional immunoassays for instance enzyme-linked immunosorbent assay, fluorescence immunoassay and electrochemical immunoassay were commonly used to determine proteins with reliability and specificity, the tedious steps, long assay time and insufficient sensitivity restricted their application in rapid and sensitive POCT (Wang et al., 2018a).

Proximity hybridization assay (PHA), a newly developed DNA-assisted protein assay strategy, paved a promising way for the acquisition of more faster POCT in clinical diagnosis (Wang et al., 2018b; Malhotra et al., 2010). Through a pair of DNA-antibody affinity probes, the recognization of target antigen and the hybridization of DNA-conjugated probes were simultaneously realized for further triggering the detection signal (Gomez de la Torre et al., 2012; Nong et al., 2013). Based on the one-step recognize procedure, not only the limitations of complex and time-consuming procedure can be well overcame, but also DNA signal amplification strategies can be introduced to improve the sensitivity (Huang et al., 2019). Therefore, various

* Corresponding author. College of Chemistry and Materials, Fujian Normal University, Fuzhou, Fujian, 350108, China.
*E-mail address:* dhong@fjnu.edu.cn (H. Dai).
[1] The author contributed to the work equally and should be regarded as co-first author.

https://doi.org/10.1016/j.bios.2020.112201
Received 7 January 2020; Received in revised form 19 March 2020; Accepted 6 April 2020
Available online 10 April 2020

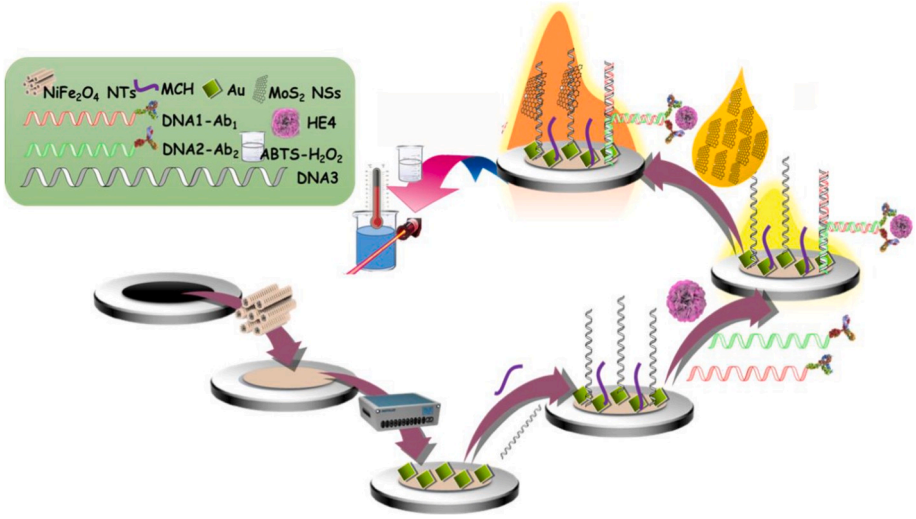


**Scheme 1.** Schematic illustration of the proximity hybridization-based multiple stimuli-responsive immunosensing platform.

proximity hybridization-regulated immunosensing strategies were proposed combined different detection technologies such as photoelectrochemistry (Wen and Ju, 2016), electrochemistry (Zhang et al., 2007), chemiluminescence (Liu et al., 2016) and fluorescencence (Zou et al., 2017). Notwithstanding adequate sensitivity and high selectivity were realized in above-developed approaches, the inherent defects of traditional single-signal output mode induced by inevitable systematic error and ambient interference might lead to the false-positive or false-negative results (Zhang et al., 2014; Jiménez et al., 2004). To improve the exactness and diversity of analysis for meeting different needs in protein detection, multi-signal readout biosensor, which simultaneously output multiple signals for target analysis, is extremely required.

Among these existing analytical techniques, both electrochemiluminescence (ECL), colorimetric assay and photothermal detection are appealing particular interest owing to their attractive advantages. To be specific, ECL with integrated superiority of electrochemistry and chemiluminescence is free of excitation light source and complicated instrumentation, which makes it become an powerful approach for trace protein detection because of its low background, high sensitivity, simple operation and good controllability (Wang et al., 2016; Xia et al., 2015). Colorimetric method possesses the merits of simplicity, practicality, rapidity, and is convenient to obtain on-site visual analysis (Wang et al., 2018a; Gao et al., 2013). In addition, photothermal sensing quantitatively monitors the photothermal effect-triggered heat by a common thermometer (Fu et al., 2018; Wei et al., 2019). Owing to the easily available common devices, facile signal readout, and rapid analytical process (Liu et al., 2019b), the development of photothermal immunosensor is particularly promising in POCT. With these in mind, a proximity hybridization-regulated multi-signal readout format was conceived in this work.

Indubitably, one material with multiple functions for enhancing or triggering the signals of ECL, colorimetric and photothermal sensing plays a vital role in the fabrication of this multi-model sensing platform, which can effectively avoid the shortcomings based on diverse materials such as complex-functional process, time-consuming, high-cost and unavoidable interference. $MoS_2$ nanosheets ($MoS_2$ NSs), a graphene-like two-dimensional atomically layered nanomaterial, has drawing tremendous attention in different fields benefited from its easy functionalization (Su et al., 2019), large surface area (Jin et al., 2016), good biocompatibility (Su et al., 2019), favorable electrocatalytic activity (Yang et al., 2015), remarkable photothermal effect (Yin et al., 2014) and outstanding peroxidase-like activity (Chen et al., 2017). Accordingly, the manifold advantageous attributes of $MoS_2$ NSs endow it be a promising candidate in this exploration. Concretely, in the ECL sensing, $MoS_2$ NSs can be served as a dual-enhancer because that its good electrocatalytic property expedited the ECL process between luminol (the luminophore) and dissolved oxygen, and good photothermal effect under the near-infrared (NIR) light converted laser energy to heat for increasing the electrochemical reaction rate (Chen et al., 2007; Lin et al., 2007; Fang et al., 2019), which greatly improved the luminol emission signal for high sensitive detection of target. Besides, the excellent peroxidase-like activity of $MoS_2$ NSs makes it as nanozyme to trigger the oxidation of 2,2′-azinobis(3- ethylbenzothiazoline)-6-sulfonic acid (ABTS) for oxidizing ABTS ($ABTS^{\bullet+}$) in the presence of $H_2O_2$ and causing the visual color change from colourless to green, which induced the colorimetric detection. Exhilaratingly, another useful and interesting feature of the green $ABTS^{\bullet+}$ tuned by $MoS_2$ NSs was its strong NIR laser-driven photothermal effect, which can be used as sensitive photothermal probe to trigger the photothermal immunosensing. Furthermore, the strong interaction between $MoS_2$ NSs and single-stranded DNA (ss-DNA) benefited from van der Waals (vdW) force (Luan and Zhou, 2018; Lu et al., 2017) was propitious to the convenient and specific absorption of $MoS_2$ NSs onto the sensing surface and avoided the tedious chemical modification process.

Inspired by all above perspectives, a split-type proximity hybridization-regulated multi-responsive biosensing strategy enhanced or triggered by $MoS_2$ NSs was devised and human epididymis-specific protein 4 (HE4), a typical ovarian carcinoma biomarker (Granato et al., 2015), was selected as the model protein to demonstrate the feasibility of this design (Scheme 1). The sensing principle was depicted in Scheme 1. Initially, $NiFe_2O_4$ nanotubes (NTs) with large surface area and unique electronic conductivity (Wang et al., 2019; Ma et al., 2016) was dropped onto the electrode surface as the immunosensor sensing platform for improving the analytical capacity. Next, electrodeposited Au nanoparticles (ed-Au NPs) were obtained on the above matrix by potential stripping strategy (Zhang et al., 2015). Then the thiolated capture DNA (DNA3, Table S1) was self-assembled onto the above modified electrode by Au–S bond to form the sensing recognition platform. In the presence of target HE4, the immunological recognition happened between HE4 and a pair of DNA-labeled antibody probes (DNA1-Ab1 and DNA2-Ab2) accompanying with the formation of proximity hybridization among DNA3, DNA1-Ab1 and DNA2-Ab2 on the sensing matrix. After sandwich immunoassay and proximity hybridization, $MoS_2$ NSs was adsorbed onto the electrode surface by virtue of the vdW force between $MoS_2$ NSs and ss-DNA. Ultimately, the obtained resultant electrode was used to change the ECL signal of luminol in the ECL test solution and the residual $MoS_2$ NSs (r-$MoS_2$ NSs) after

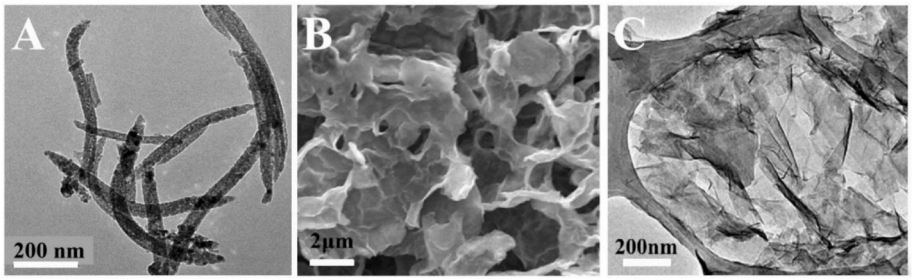


**Fig. 1.** (A) TEM of $NiFe_2O_4$ NTs. SEM (B) and TEM (C) of $MoS_2$ NSs.

absorbance by ss-DNA was served as the trigger for the subsequent colorimetric analysis and photothermal sensing. With the increasing of target HE4, the amount of hybridized double-stranded DNA (ds-DNA) also increased, thus, the lesser $MoS_2$ NSs can be absorbed onto the electrode surface and more r-$MoS_2$ NSs was remained in the soaking solution, leading to the decrease of ECL signals and the increase of colorimetric and photothermal effect. Therefore, the quantitative analysis of target HE4 was realized by recording the alterations of output signals, which can provide more accurate result by the mutual calibration of different modes.

## 2. Experimental section

### 2.1. Material, reagents and apparatus

Reagents, apparatus, oligonucleotides, the synthesis of $NiFe_2O_4$ NTs (Wang et al., 2019) and $MoS_2$ NSs (Jia et al., 2019), and the preparation (Wang et al., 2018b; Huang et al., 2019) of hybridized DNA-labeled antibodies (DAN1-Ab1, DNA2-Ab2, Fig. S1) were displayed in Supporting Information.

### 2.2. Construction of the biosensor

Initially, 4 μL of 2 mg/mL $NiFe_2O_4$ NTs was deposited onto the pretreated glassy carbon electrode (GCE, d = 3 mm) and dried under infrared lamp. After cooled to room temperature, the above electrode was immersed in 1% (wt) $HAuCl_4$ solution for electrochemical deposition at -0.2 V for 15 s to obtain GCE/$NiFe_2O_4$ NTs/ed-Au NPs (Zhang et al., 2015). Subsequently, DNA3 was immobilized onto the above electrode by dropping 10 μL of 10 μM DNA3 solution and incubating for 3 h. After the GCE/$NiFe_2O_4$ NTs/ed-Au NPs/DNA3 was immersed into 50 μL of 1 mM 6-mercapto-1-hexanol (MCH) solution for 30 min to block the nonspecific binding sites, 30 μL of 55 mM PBS2 containing 13 nM DNA1-Ab1, 13 nM DNA2-Ab2 and different concentration of HE4 was drop-coated the above electrode and incubated for 1 h at 37 °C to obtain the GCE/$NiFe_2O_4$ NTs/ed-Au NPs/DNA3/DNA-Ab-HE4. Finally, the modified electrode was dipped into 20 μL of 2 mg/mL $MoS_2$ solution for 30 min at room temperature to accomplish the adsorption between ss-DNA and $MoS_2$ NSs for acquire the resultant electrode (GCE/$NiFe_2O_4$ NTs/ed-Au NPs/DNA3/DNA-Ab-HE4/$MoS_2$ NSs). The residual $MoS_2$ solution (r-$MoS_2$) after above absorption process was stored for the subsequent colorimetric and photothermal analysis. At each step, the electrode was rinsed with 10 mM PBS3 (0.01M $Na_2HPO_4$, 0.01M $NaH_2PO_4$, pH 7.4) to remove the excess reagents.

### 2.3. Measurement process

In the ECL sensing process, conventional three-electrode system was adopted with Ag/AgCl electrode as reference electrode, platinum wire with as auxiliary electrode, and the above resultant electrode (GCE/$NiFe_2O_4$ NTs/ed-Au NPs/DNA3/DNA-Ab-HE4/$MoS_2$ NSs) as working electrode. The 0.1 M PBS4 (0.1 M $Na_2HPO_4$, 0.1 M $NaH_2PO_4$, pH 8.0) containing $10^{-5}$ M luminol was employed as test solution. The ECL measurements were conducted using a commercial ECL system with a scanning range of 0–1.2 V and the voltage was set to 800 V after the resultant electrode irradiated by 808 nm infrared light (2.5 W/$cm^2$) for 40 s (the layout was displayed in Scheme S1).

Before the colorimetric and photothermal analysis, the above r-$MoS_2$ solution was firstly stirred for 2 min and then transferred 15 μL solution into a 0.5 mL PCR tube. Afterwards, 385 μL mixed solution containing ABTS (0.4 mM) and $H_2O_2$ (1.0 M) was added into the above PCR tube. After reacting for 2 min, the color of the system was from colorless to green-colored, which was recorded by using a digital camera. Subsequently, 200 μL resultant solution was removed into micro cuvette to monitor the absorbance of this system on UV-1900 spectrophotometer from 400 nm to 850 nm and the absorbance at 415 nm ($A_{415}$) was recorded.

The 200 μL remain green-colored solution in 0.5 mL PCR tube was used to perform the photothermal detection. Before the irradiation of the laser, the solution temperature was firstly recorded by the pen-style digital thermometer by inserting it into the solution. Then the green-colored solution in PCR tube was irradiated vertically under 808 nm laser at the power density of 2.5 W/$cm^2$ for 30 s and the thermometer was immediately inserted into the solution to obtain the highest steady temperature. Finally, the temperature increasement was recorded for the quantitative analysis of target HE4.

## 3. Results and discussion

### 3.1. Characterization of $NiFe_2O_4$ NTs and $MoS_2$ NSs

To reveal the morphology and size of the as-synthesized materials, transmission electron microscopy (TEM) and scanning electron microscopy (SEM) were carried out. From the TEM image of $NiFe_2O_4$ NTs in Fig. 1A, slightly curved hollow framework constructed by many small nanoparticles was clearly displayed, demonstrating the unique tubular structure of $NiFe_2O_4$ NTs with the length of about 400–650 nm, which is accordance with the result of previous reports (Wang et al., 2019). Besides, the SEM image in Fig. 1B shows massive large-scale slightly wrinkled nanosheets, which indicated that the prepared $MoS_2$ NSs possesses two-dimensional sheet structure. Furthermore, nearly transparent sheets with fine edges in Fig. 1C further demonstrate the ultrathin nanosheet morphology, which implying that $MoS_2$ NSs can provide more active sites for subsequent application.

### 3.2. Exploration the versatile capability of $MoS_2$ NSs

Owing to the vital role of $MoS_2$ NSs in this multi-readout sensing platform, a series of experiments without immunoassay process (detailed operation description was listed in SI) were carried out to investigate the multiple functions of $MoS_2$ NSs. Accordingly, the practicability of $MoS_2$ NSs regulated ABTS-$H_2O_2$ chromogenic system was firstly explored by studying its colorimetric and optical properties (Zou et al., 2019; Fan et al., 2017; Lee et al., 2005). As demonstrated in Fig. 2A, there was no apparent color alteration in these PCR tubes (a-f) without $MoS_2$ NSs, ABTS, or $H_2O_2$, while obvious green color (g) was

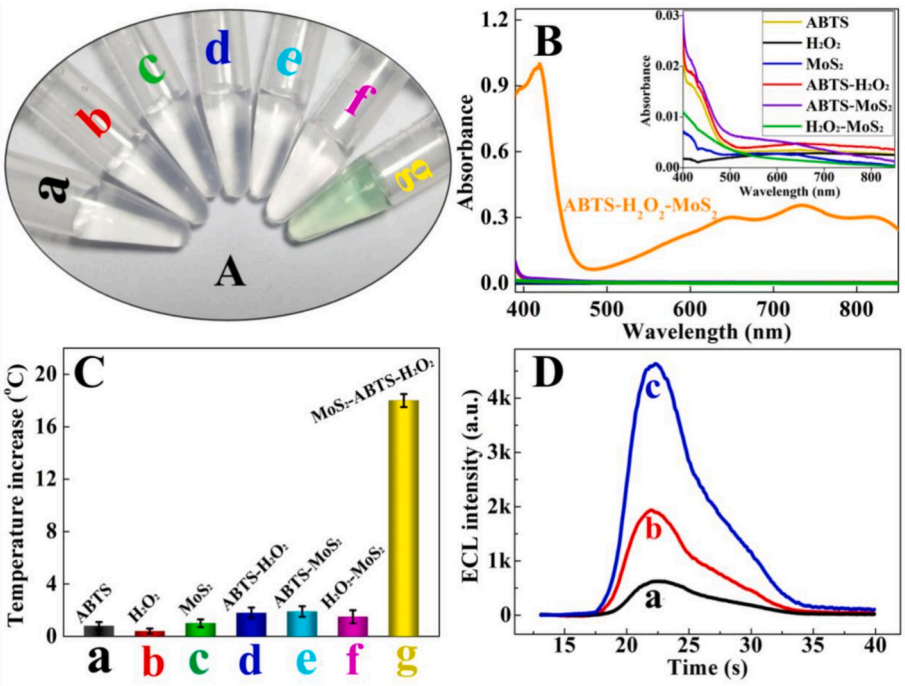


**Fig. 2.** Photographs (A) and UV–vis absorption spectra (B) of different components in $MoS_2$ NSs mediated ABTS-$H_2O_2$ colorimetric system. (C) Temperature changes of the corresponding reaction solutions (0.2 mL) after irradiating by an 808 nm laser (2.5 W $cm^{-2}$) for 30 s. (D) ECL responses of (a) GCE and (b) GCE/$MoS_2$ NSs without and (c) GCE/$MoS_2$ NSs with 808 nm laser (2.5 W $cm^{-2}$) irradiation for 40 s in 0.1 M PBS4 (0.1 M $Na_2HPO_4$, 0.1 M $NaH_2PO_4$, pH 8.0) containing $10^{-5}$ M luminol. a-f in (A) and (C) was corresponding with each other.

exhibited only with the appearance of $MoS_2$ NSs, ABTS, and $H_2O_2$, which is accordance with the result of previous ABTS-$H_2O_2$ colorimetric system (Zou et al., 2019). The color alteration from colorless to green was attributed to that $MoS_2$ NSs catalyzed the oxidation of colorless ABTS in the presence of $H_2O_2$ to produce green-colored $ABTS^{\bullet+}$ via single-electron transfer. The results not only confirmed the effective catalysis of $MoS_2$ NSs to the ABTS-$H_2O_2$ chromogenic reaction, but also preliminary heralded that the $MoS_2$ NSs-induced ABTS-$H_2O_2$ colorimetric system can be successful constructed. Furthermore, a remarkable UV–vis absorption peak was appeared at around 415 nm, 650 nm, 732 nm and 820 nm (Fig. 2B) only in the green color solution, which is assigned to the characteristic absorption peak of $ABTS^{\bullet+}$ (Fan et al., 2017; Lee et al., 2005). Interestingly, a significant increasement of $ABTS^{\bullet+}$ absorbance from 500 nm to 850 nm was observed in Fig. 2B, implying the good near-infrared absorption property of $ABTS^{\bullet+}$ and indicating the possibility of $MoS_2$ NSs-mediated ABTS-$H_2O_2$ chromogenic system for photothermal application.

For investigating the outstanding photothermal effect of $MoS_2$ NSs-regulated ABTS-$H_2O_2$ colorimetric system, all the reaction solutions in PCR tubes were irradiated by 808 nm laser with the power density of 2.5 W/$cm^2$ for 30 s and recorded the temperature changes of reaction solutions by virtue of a pen-style digital thermometer. Strikingly, comparing with the unconspicuous temperature changes in colorless solutions, the $MoS_2$ NSs-stimulated ABTS-$H_2O_2$ chromogenic solution (g) presented the biggest temperature variation (16.8 °C) in Fig. 2C. The phenomena can be explained by the significant NIR laser-irradiated photothermal performance of the colorimetric system derived from the strong NIR light absorption of $ABTS^{\bullet+}$, which was well accordance with the result in Fig. 2B. The results make us believe that $ABTS^{\bullet+}$ can serve as an excellent photothermal agent to convert the adsorbed NIR light into heat (Fig. S2), which offered guidance on exploring novel photothermal probes and designing ingenious photothermal sensing platform.

Besides, the dual-sensitive function for the cathodic ECL emission of luminol was also researched. As demonstrated in Fig. 2D, a higher ECL signal was observed at GCE/$MoS_2$ NSs (curve b, 1925 a.u.) in 0.1 M PBS4 containing $10^{-5}$ M luminol compared with that of GCE (curve a, 602 a.u.). The nearly 3-fold enhancement was mainly derived from the good electrocatalytic activity of $MoS_2$ NSs, which made it used as an effective co-reaction accelerator in the luminol-$O_2$ system (Figs. S3 and S4) to catalyze the decomposition of dissolved $O_2$ for producing more superoxide anion ($O_2^{\bullet-}$). Moreover, the sulfur vacancies in $MoS_2$ NSs make the adjacent Mo atoms expose to the material surface with uncoordinated format, which was employed as active sites to absorb more dissolved $O_2$, further improving the electrocatalytic property of $MoS_2$ NSs (Sun et al., 2019). As expected, the strongest ECL response was obtained at the 808

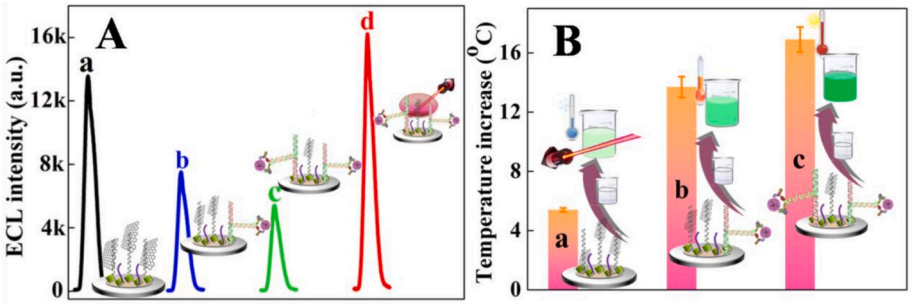


**Fig. 3.** (A) ECL intensities of (a) GCE/$NiFe_2O_4$ NTs/ed-Au NPs/DNA3/$MoS_2$ NSs, (b, c) GCE/$NiFe_2O_4$ NTs/ed-Au NPs/DNA3/DNA-Ab-HE4/$MoS_2$ NSs without and (d) GCE/$NiFe_2O_4$ NTs/ed-Au NPs/DNA3/DNA-Ab-HE4/$MoS_2$ NSs with 808 nm laser irradiation (2.5 W $cm^{-2}$) for 40 s. The HE4 concentrations were 1 ng/mL (b) and 10 ng/mL (c, d), respectively. (B) The temperature increases of oxidized ABTS-$H_2O_2$ colorimetric system induced by the corresponding r-$MoS_2$ (a, b, c) in Figure A.

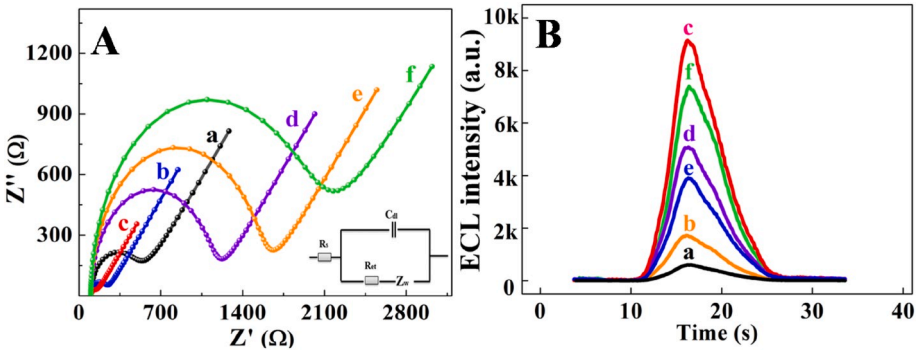


**Fig. 4.** (A) EIS of different electrodes in 0.1 M KCl solution containing 5.0 mM $[Fe(CN)_6]^{3-/4-}$. The inset is the equivalent circuit for EIS. (B) ECL responses of corresponding modified electrodes in 0.1 M PBS4 (0.1 M $Na_2HPO_4$, 0.1M $NaH_2PO_4$, pH 8.0) containing $10^{-5}$ M luminol. (a) GCE, (b) GCE/$NiFe_2O_4$ NTs, (c) GCE/$NiFe_2O_4$ NTs/ed-Au NPs, (d) GCE/$NiFe_2O_4$ NTs/ed-Au NPs/DNA3, (e) GCE/$NiFe_2O_4$ NTs/ed-Au NPs/DNA3/DNA-Ab-HE4 and (f) GCE/$NiFe_2O_4$ NTs/ed-Au NPs/DNA3/DNA-Ab-HE4/$MoS_2$ NSs. The HE4 concentration was 0.1 ng/mL.

nm laser irradiated GCE/$MoS_2$ NSs (cure c, 4637 a.u.). The remarkable enhanced ECL response was originated from the good photothermal property of $MoS_2$ NSs which elevated the electrode temperature, leading to the decrease in viscosity around the electrode surface and further accelerating the diffusion between electroactive species and electrode (Chen et al., 2009).

Exhilaratingly, such phenomena all verified the presumption that three different output signals can be triggered or enhanced by the multifunctional $MoS_2$ NSs, which provided a key precondition for the fabrication of the multi-readout sensing platform.

### 3.3. Feasibility assessment of the sensing tactic in PHA immunosensor for multi-model readout

To evaluate the feasibility of the sensing strategy in this PHA immunosensor, the cathodic ECL responses of luminol to different modified electrodes (Fig. 3A) and the corresponding temperature changes of green-colored $ABTS^{\bullet+}$ solutions with the laser irradiation for 30 s (Fig. 3B) were recorded by using HE4 as model target. The ECL intensity of luminol at GCE/$NiFe_2O_4$ NTs/ed-Au NPs/DNA3 was only 5083 a.u. (Fig. 5B, curve d), while after the modified electrode was soaked by 20 μL of 2 mg/mL $MoS_2$ solution for 30 min, a higher ECL intensity (13590 a.u., curve a) was observed in Fig. 3A. The significantly enhanced ECL signal was mainly originated from that many $MoS_2$ NSs was absorbed onto the modified electrode by the vdW force between ss-DNA and $MoS_2$ NSs, which used the effective electrocatalytic activity for luminol emission process to improve the ECL response (Figs. S3 and S4). When the GCE/$NiFe_2O_4$ NTs/ed-Au NPs/DNA3 was immersed into the mixed solution including DNA1-Ab1, DNA2-Ab2 and HE4 for 60 min, the proximity hybridization was occurred (Figs. S6 and S7) and the ds-DNA was formed, thus the lesser $MoS_2$ NSs can be absorbed onto the electrode and the lower ECL response was obtained. As depicted in Fig. 3A, with the increasing of HE4 concentration from 1 ng/mL (curve b) to 10 ng/mL (curve c), the amount of ss-DNA decreased and the ECL signal also successively diminished, which predicted the possibility of ECL sensing for HE4 detection. More importantly, comparing with the ECL intensity at the ultimate modified electrode without laser irradiation (curve c), a remarkable improved signal (curve d) was acquired after that the same electrode was irradiated by 808 nm laser for 40 s. The result can be explained by the fact that the elevated temperature induced by good photothermal convert performance of $MoS_2$ NSs (Fig. S5) improved the cathodic emission of luminol.

Similarly, without the presence of ds-DNA at the modified electrode, the more $MoS_2$ NSs was absorbed onto the electrode and the lesser r-$MoS_2$ was remained in the soaking solution, which leaded to the lesser oxidation of ABTS and the lower temperature change (Fig. 3B, histogram a). Accompanying with the increasing of ds-DNA derived from the increasing HE4 concentration, more and more r-$MoS_2$ was left and much more $ABTS^{\bullet+}$ was produced, resulting in the deeper green-colored appeared and the higher temperature change (histogram b and c). All above the results (Fig. 3A and B) not only demonstrated the successful occurrence of proximity hybridization initiated by the target antigen, but also validated the affinity discrepancy of $MoS_2$ NSs to ssDNA and ds-DNA, which implying the sensing tactic can possibly be employed to quantitative monitor the concentration of tumor biomarkers.

### 3.4. Characterizations for the construction of the immunosensor

As a proof-of-concept application, this multi-model PHA biosensor based on versatile $MoS_2$ NSs was firstly fabricated. The corresponding variations of stepwise assembly process were monitored by electrochemical impedance spectroscopy (EIS) and ECL measurements in Fig. 4 to attest the successful preparation of this sensor. As illustrated in Fig. 4A, smaller and smaller semicircles were appeared after $NiFe_2O_4$ NTs (curve b) and Au NPs (curve c) were orderly decorated onto electrode surface compared with that of bare GCE (curve a), which was resulted from the good conductive property of $NiFe_2O_4$ NTs (Wang et al., 2019) (Fig. S3C) and ed-Au NPs (Zhang et al., 2015), which served as conducting bridges and made electrons transfer between the electroactive probes and the electrode more easily. As expected, the resistances increased successively when DNA3 (curve d), DNA-Ab-HE4 (curve e), and $MoS_2$ NSs (curve f) were orderly anchored onto the above electrode surface. The reason was mainly attributed to that the repulsion between the negatively charged phosphate groups in DNA and $[Fe(CN)_6]^{3-/4-}$, the insulative property of immunocomplex and the low conductivity of $MoS_2$ NSs retarded the diffusion of electroactive probes to the electrode surface. Such changes in Fig. 3A certified the successful construction of this immunosensor.

Furthermore, the ECL responses of different modified electrodes were investigated in 2 mL of 0.1 M PBS4 (pH 8.0) containing $10^{-5}$ M luminol in Fig. 4B. Distinctly, the $NiFe_2O_4$ NTs presented a higher ECL signal (1853 a.u., curve b) which was nearly 3-fold higher than that of GCE (602 a.u., curve a). The elevated ECL intensity was mainly ascribed to the good catalytic performance of $NiFe_2O_4$ NTs for oxygen evolution reaction (OER) process to generate $O_2$ (Fig. S4C) (Wang et al., 2019), which played an crucial role in the cathodic ECL emission of luminol (Fig. S4D). Excitingly, a highest ECL response (9153 a.u.) was occurred at GCE/$NiFe_2O_4$ NTs/ed-Au NPs (curve c) benefited from the excellent conductivity of Au, which implied that Au NPs was successful electrodeposited onto the electrode surface. Subsequently, the ECL signals gradually decreased with the immobilization of DNA3 (curve d) and DNA-Ab-HE4 (curve e) due to the impeditive effect of DNA and proteins, indicating the successful capture of DNA and the successful hybridization triggered by HE4. Not surprisingly, the ECL response improved after that $MoS_2$ NSs was absorbed (curve f) onto the above electrode because of the catalytic effect of $MoS_2$ to luminol emission (Figs. S3 and S4). The phenomenon not only demonstrated the successful fabrication of immunosensor, but also certified the feasibility of ECL sensing format for protein determination.

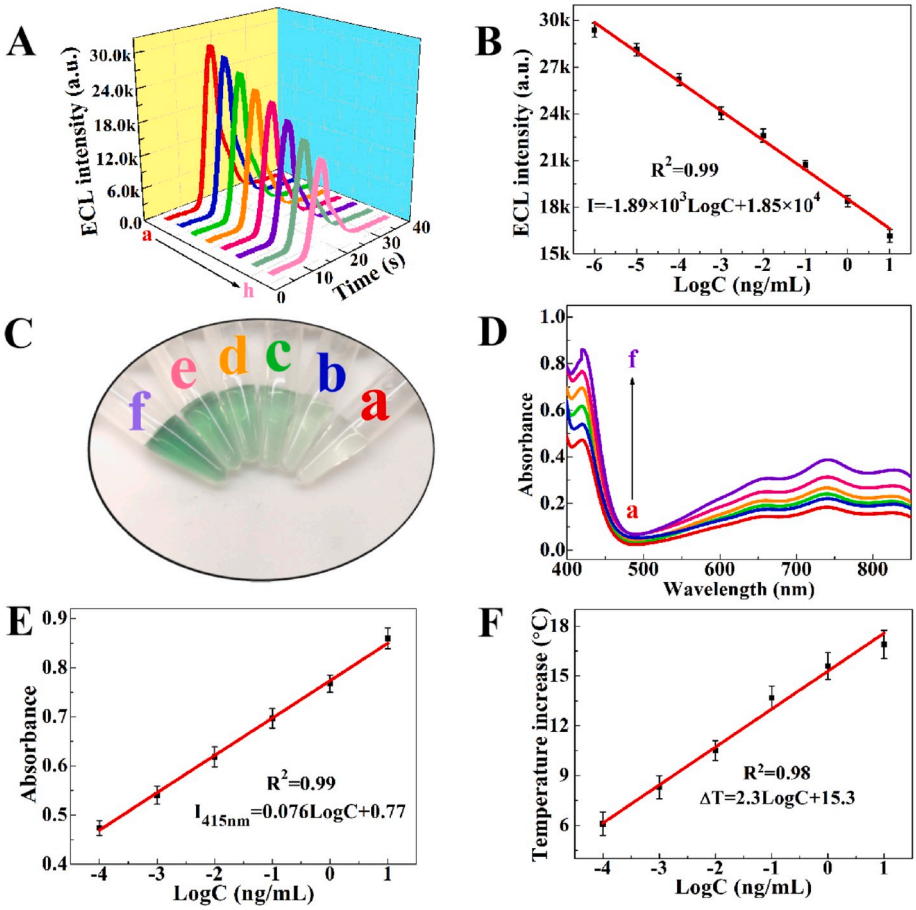


**Fig. 5.** ECL-time profiles (A) and Calibration curve (B) of ECL biosensor at different HE4 concentrations from (a) $10^{-6}$ ng/mL to (h) 10 ng/mL. Photographs (C) and UV–vis absorption spectra (D) of the colorimetric system obtained from different HE4 concentrations in the range from (a) $10^{-4}$ ng/mL to (f) 10 ng/mL. Linear plots of (E) UV–vis absorbance at 415 nm and (F) temperature increase versus the logarithm of HE4 concentration.

### 3.5. Conditional optimization

To acquire the excellent analytical performance, all experimental conditions in the preparation and detection process were optimized. As exhibited in Fig. S8, the maximum ECL responses were obtained in 2 mg/mL $NiFe_2O_4$ NTs (Fig. S8A), 10 s electrodeposited time (Fig. S8B), 3 h DNA3 capture time (Fig. S9A, red line), 60 min hybridized time (Fig. S9B, blue line), 30 min $MoS_2$ NSs absorbed time (Fig. S9C), respectively.

Besides, the laser irradiate time is also important to the signal output and biological activity of protein, so the time of 808 nm laser irradiation were investigated. The optimal irradiate time of the prepared electrode was 40 s (Fig. S9D) and the 30 s was selected as the ultimate irradiate time in the $MoS_2$ NSs regulated ABTS-$H_2O_2$ colorimetric system (Fig. S10).

### 3.6. Multiple readout of immunosensing by ECL, colorimetric and temperature

Different concentrations of HE4 were prepared and detected by the proposed immunosensor under the optimized experimental conditions. As displayed in Fig. 5A and B, with the increasing of HE4, more ds-DNA were formed and lesser $MoS_2$ NSs were absorbed onto the ECL biosensor for smaller ECL signal. Owing to the affinity between ss-DNA and $MoS_2$ NSs also causes the decrease of r-$MoS_2$ amount in the soaking solution, the r-$MoS_2$ increased with the increment of HE4. Therefore, the UV–vis absorption spectra triggered by r-$MoS_2$ and the temperature increases induced by the strong NIR light absorption of $ABTS^{\bullet+}$ are also recorded in the presence of HE4 with different concentrations. As expected, with more HE4, more r-$MoS_2$ are participated in the ABTS-$H_2O_2$ chromogenic system and more green $ABTS^{\bullet+}$ are produced (Fig. 5C), resulting in more stronger absorbance (Fig. 5D and E) and more higher temperature increases (Fig. 5F). Additionally, the detailed linearity between the detected signals (ECL intensity, absorption in 415 nm and temperature changes) and the logarithm of HE4 concentration (C, ng/mL) are demonstrated in Fig. 5B, E, F, respectively. Distinctly, the ECL assay (Fig. 5B) shows the wider linear range ($10^{-6}$ ng/mL to 10 ng/mL) and the lower detection limit ($3 \times 10^{-7}$ ng/mL, S/N = 3) than that ($10^{-4}$ ng/mL to 10 ng/mL, $3 \times 10^{-5}$ ng/mL) of colorimetric analysis (Fig. 5E) and photothermal sensing (Fig. 5F). The phenomena can be explained by that the lesser r-$MoS_2$ NSs are remained in soaking solution with the presence of the lesser HE4, leading to the lesser $ABTS^{\bullet+}$ generated which can't induce the obvious change of absorbance and temperature. Unquestionably, the results also verify the inherent merits including high sensitivity and ultralow detection limit of ECL technology. Furthermore, the corresponding regression equations and correlation coefficient ($R^2$) are described as

$$I/\text{counts (ECL intensity)} = 1.89 \times 10^3 \text{ LogC} + 1.85 \times 10^4 \ (R^2 = 0.99) \quad (1)$$

$$A_{415nm} \text{ (Colorimetric absorbance)} = 0.076 \text{ LogC} + 0.77 \ (R^2 = 0.99) \quad (2)$$

$$\Delta T/^{\circ}C \text{ (Temperature increase)} = 2.3 \text{ LogC} + 15.3 \ (R^2 = 0.98) \quad (3)$$

Comparing with other strategies for HE4 quantitative analysis, the multiple stimuli-responsive PHA sensing platform possess better accuracy originated from the connatural feature of multi-signal readout and more reliable analytical performance (Table S1).

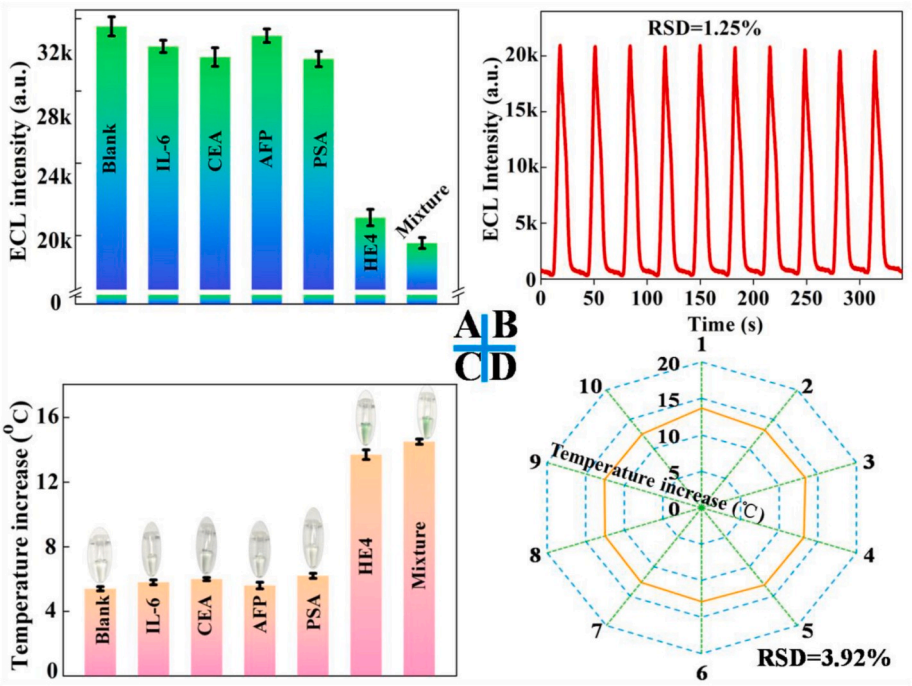


**Fig. 6.** The selectivity of the multi-signal readout platform in (A) ECL sensing and (C) photothermal analysis. The concentration of HE4 was 0.1 ng/mL, the concentrations of interferences were 10 ng/mL (B, D) Corresponding stability of the proposed biosensor for the detection of 0.1 ng/mL HE4. The insets in C were the corresponding photographs of the colorimetric system.

In order to explore the selectivity of the sensing platform for HE4 determination, the common tumor markers (IL-6, CEA, AFP, and PSA) in serum were selected as interference. As exhibited in Fig. 6A and C, the interference group (10 ng/mL) show the similar signal value compared with that of blank solution. Significant reduction of ECL signal, increasement of temperature change and obvious color change of colorimetric solution appeared when 0.1 ng/mL HE4 was present, confirming the outstanding anti-interference ability. Besides, there was no obvious decline of ECL responses (Fig. 6B) and temperature increase (Fig. 6D) under consecutive scans for 10 cycles at 0.1 ng/mL HE4, indicating the acceptable stability of multi-readout PHA immunosensor.

### *3.7. Detection of HE4 in human serums*

For estimating the practical applicability of the developed strategy, the ECL and temperature change signals were used to determine the HE4 concentration in diluted serum samples. The enzyme-linked immunosorbent assay (ELISA) as reference was employed to analysis HE4 concentration in serum samples and the results were displayed in Table S4. The detection results between ELISA and this multi-readout sensing demonstrated that the multi-signal biosensor was reliable for the analysis of serum samples. Besides, to further confirm the accuracy of this multi-signal sensing strategy in HE4 detection, one serum sample was chosen to perform the recovery experiments and the result was displayed in Table S3. The recoveries were ranged from 95.7% to 108.8% and the relative standard deviation (RSD) was lower than 5.18%, indicating the potential applications of this PHA biosensor in real samples analysis.

## 4. Conclusions

In conclusion, with creatively introduced versatile $MoS_2$ NSs by virtue of the vdW force between ss-DNA and $MoS_2$, an attractive split-type multi-element response platform including ECL, colorimetric and temperature was designed for ovarian cancer biomarker detection in human serum. As demonstrated, the sensing device displayed prominent performance including good selectivity, stability, reproducibility and high sensitivity and the false-positive or false-negative results could be effectively avoided by the mutual calibration of multiple signals. In comparison with other multi-readout immunosensor, multiple signals were triggered from or improved by the same material ($MoS_2$ NSs) in this work, which greatly simplifies the functionalized process and reduces the overaccumulation and abnormal usages of nanomaterials, meeting the economical requirements. Impressively, the innovative $MoS_2$-regulated ABTS-$H_2O_2$ photothermal sensing strategy operated with a common thermometer may inspire researchers to seek different functional materials or colorimetric systems with good photothermal performance for realizing faster and more accurate POCT.

## Declaration of competing interest

The authors declare that they have no known competing financial interests or personal relationships that could have appeared to influence the work reported in this paper.

## Acknowledgements

This work was supported by the National Natural Science Foundation of China (No. 21877012 and No. 21575024), the Joint fund of Department of education- Department of health of Fujian Province(No.2019-WJ-04).

## Appendix A. Supplementary data

Supplementary data to this article can be found online at https://doi.org/10.1016/j.bios.2020.112201.

## References

Chen, Y.T., Lin, Z.Y., Chen, J.H., Sun, J.J., Zhang, L., Chen, G.N., 2007. J. Chromatogr. A 1172, 84–91.
Chen, L.C., Chi, Y.W., Zheng, X.X., Zhang, Y.J., Chen, G.N., 2009. Anal. Chem. 81, 2394–2398.

Chen, Q.A., Chen, H., Li, Z.H., Pang, J., Lin, T., Guo, L.Q., Fu, F.F., 2017. J. Nanosci. Nanotechnol. 17, 5730–5734.
Fan, W.J., Qiao, J.L., Guan, X.H., 2017. Chemosphere 171, 460–467.
Fang, D.D., Zhang, S.P., Dai, H., Lin, Y.Y., 2019. Biosens. Bioelectron. 146, 111768–111772.
Fu, G.L., Sanjay, S.T., Zhou, W., Brekken, R.A., Kirken, R.A., Li, X.J., 2018. Anal. Chem. 90, 5930–5937.
Gao, Z.Q., Xu, M.D., Hou, L., Chen, G.N., Tang, D.P., 2013. Anal. Chem. 85, 6945–6952.
Gao, H.F., Wang, X.F., Li, M., Qi, H.L., Gao, Q., Zhang, C.X., 2017. Biosens. Bioelectron. 98, 62–67.
Gomez de la Torre, T.Z., Ke, R.Q., Mezger, A., Svedlindh, P., Stromme, M., Nilsson, M., 2012. Small 8, 2174–2177.
Granato, T., Porpora, M.G., Longo, F., Angeloni, A., Manganaro, L., Anastasi, E., 2015. Clin. Chim. Acta 446, 147–155.
Huang, X.C., Zhang, Y., Xu, W., Xu, W., Guo, L.H., Qiu, B., Lin, Z.Y., 2019. Chem. Commun. 55, 12980–12983.
Jia, X.H., Huang, J., Li, Y., Yang, J., Song, H.J., 2019. Appl. Surf. Sci. 494, 430–439.
Jiménez, D., Martínez-Máñez, R., Sancenón, F., Soto, J., 2004. Tetrahedron Lett. 45, 1257–1259.
Jin, K., Xie, L.M., Tian, Y., Liu, D.M., 2016. J. Phys. Chem. C 120, 11204–11209.
Lee, Y., Yoon, J., von Gunten, U., 2005. Water Res. 39, 1946–1953.
Li, H., He, J., Li, S.J., Turner, A.P.F., 2013. Biosens. Bioelectron. 43, 25–29.
Lin, Z.Y., Sun, J.J., Chen, J.H., Guo, L., Chen, G.N., 2007. Electrochem. Commun. 9, 269–274.
Liu, M.M., Wu, J., Yang, K.L., Zong, C., Lei, J.P., Ju, H.X., 2016. Talanta 154, 455–460.
Liu, B., Wang, K., Gao, B.B., Lu, J., Li, H.M., Zhao, X.W., 2019a. ACS Appl. Nano Mater. 2, 3177–3186.
Liu, X.F., Zou, L.Y., Yang, X.H., Wang, Q., Zheng, Y., Geng, X.H., Liao, G.F., Nie, W.Y., Wang, K.M., 2019b. Anal. Chem. 91, 7943–7949.
Lu, C., Liu, Y.B., Ying, Y.B., Liu, J.W., 2017. Langmuir 33, 630–637.
Luan, B.Q., Zhou, R.H., 2018. ACS Nano 12, 3886–3891.
Ma, Y.D., Dai, X.P., Liu, M.Z., Yong, J.X., Qiao, H.Y., Jin, A.X., Li, Z.Z., Huang, X.L., Wang, H., Zhang, X., 2016. ACS Appl. Mater. Interfaces 8, 34396–34404.
Malhotra, R., Patel, V., Waque, J.P., Gutkind, J.S., Rusling, J.F., 2010. Anal. Chem. 82, 3118–3123.
Nong, R.Y., Wu, D., Yan, J.H., Hammond, M., Gu, G.J., Kamali-Moghaddam, M., Landegren, U., Darmanis, S., 2013. Nat. Protoc. 8, 1234–1248.
Su, S., Li, J., Yao, Y., Sun, Q., Zhao, Q., Wang, F., Li, Q., Liu, X.G., Wang, L.H., 2019. ACS Appl. Biol. Mater. 2, 292–298.
Sun, G.R., Li, F., Wu, T., Cong, L.N., Sun, L.Q., Yang, G.C., Xie, H.M., Mauger, A., Julien, C.M., Liu, J., 2019. Inorg. Chem. 58, 2169–2176.
Wang, H.J., Yuan, Y.L., Zhuo, Y., Chai, Y.Q., Yuan, R., 2016. Anal. Chem. 88, 2258–2265.
Wang, J.N., Yang, X., Wei, T.X., Bao, J.C., Zhu, Q.S., Dai, Z.H., 2018a. ACS Appl. Biol. Mater. 1, 382–388.
Wang, X.F., Gao, H.F., Qi, H.L., Gao, Q., Zhang, C.X., 2018b. Anal. Chem. 90, 3013–3018.
Wang, J.N., Song, J.R., Zheng, H.L., Zheng, X.Q., Dai, H., Hong, Z.S., Lin, Y.Y., 2019. Sens. Actuators, B 288, 80–87.
Wei, Y.Y., Wang, D.N., Zhang, Y.Z., Sui, J.H., Xu, Z.R., 2019. Biosens. Bioelectron. 140, 111345–111353.
Wen, G.M., Ju, H.X., 2016. Anal. Chem. 88, 8339–8345.
Xia, H., Li, L.L., Yin, Z.Y., Hou, X.D., Zhu, J.J., 2015. ACS Appl. Mater. Interfaces 7, 696–703.
Yang, T., Yang, R.R., Chen, H.Y., Nan, F.X., Ge, T., Jiao, K., 2015. ACS Appl. Mater. Interfaces 7, 2867–2872.
Yin, W.Y., Yan, L., Yu, J., Tian, G., Zhou, L.J., Zheng, X.P., Zhang, X., Yong, Y., Li, J., Gu, Z.J., Zhao, Y.L., 2014. ACS Nano 8, 6922–6933.
Zhang, Y.L., Huang, Y., Jiang, J.H., Shen, G.L., Yu, R., 2007. J. Am. Chem. Soc. 129, 15448–15449.
Zhang, H.R., Wu, M.S., Xu, J.J., Chen, H.Y., 2014. Anal. Chem. 86, 3834–3840.
Zhang, P., Wu, X.Y., Yuan, R., Chai, Y.Q., 2015. Anal. Chem. 87, 3202–3207.
Zou, M.Q., Li, D.X., Yuan, R., Xiang, Y., 2017. Biosens. Bioelectron. 92, 624–629.
Zou, J., Huang, Y.X., Zhu, L.R., Cui, Z., Yuan, B.L., 2019. Spectrochim. Acta, Part A 216, 214–220.